Journal of Alloys and Compounds 1047 (2025) 185124

Contents lists available at ScienceDirect

Journal of Alloys and Compounds

journal homepage: www.elsevier.com/locate/jalcom

Research article

Microstructure, crystalline orientation evolution and electromechanical properties of $0.5Ba(Zr_{0.2}Ti_{0.8})O_3-0.5(Ba_{0.7}Ca_{0.3})TiO_3$ thin films on platinized sapphire substrate

Sabi William Konsago [a,b,*], Maja Koblar [a], Katarina Žiberna [a,b], Aleksander Matavž [a], Barnik Mandal [c,d], Sebastjan Glinšek [d], Vid Bobnar [a,b], Andreja Benčan [a,b], Barbara Malič [a,b,*]

[a] Jožef Stefan Institute, Jamova cesta 39, Ljubljana 1000, Slovenia
[b] Jožef Stefan International Postgraduate School, Jamova cesta 39, Ljubljana 1000, Slovenia
[c] University of Luxembourg, 41 rue du Brill, Belvaux L-4422, Luxembourg
[d] Smart Materials Unit, Luxembourg Institute of Science and Technology, 41, rue du Brill, Belvaux L-4422, Luxembourg

ARTICLE INFO

Keywords:
$0.5Ba(Zr_{0.2}Ti_{0.8})O_3$—$0.5(Ba_{0.7}Ca_{0.3})TiO_3$ thin films
Microstructure
Crystalline orientation
Electromechanical properties

ABSTRACT

The microstructure and crystalline orientation evolution of manganese-doped $0.5Ba(Zr_{0.2}Ti_{0.8})O_3$—$0.5(Ba_{0.7}Ca_{0.3})TiO_3$ (BZT—BCT) thin films deposited on platinized sapphire and multistep-annealed at 850 °C are reported. The crack-free 680 nm thick BZT—BCT films with an average lateral grain size of 140 nm exhibit preferential {111} orientation on the surface confirmed by the electron backscatter diffraction (EBSD). Transmission Kikuchi diffraction (TKD) analysis reveals the evolution of preferential {111} and {110} orientation of columnar grains along the film thickness, that is, in the grain-growth direction. The formation of pores at the interface of the film and substrate is observed and related to the migration of pores and grain boundaries. The dielectric permittivity and losses of 840 and 0.02, respectively, at 1 kHz, are measured at room temperature. The maximum polarization and strain at an electric field of 1.2 MV•cm^{-1} are about 32 μC•cm^{-2} and 0.35 %, respectively. The piezoelectric d_{33} coefficient of 42 pm•V^{-1} was measured by double-beam laser interferometry.

1. Introduction

The design and processing of lead-free $0.5Ba(Zr_{0.2}Ti_{0.8})O_3$—$0.5(Ba_{0.7}Ca_{0.3})TiO_3$ (BZT—BCT) piezoelectric ceramics and thin films with enhanced functional properties as alternatives to lead-based materials in piezoelectric applications have been extensively studied since Liu and Ren in 2009 reported a high piezoelectric d_{33} coefficient of 620 pC·N^{-1} for this composition [1]. In general, the interest in the development of lead-free piezoelectric materials has been triggered by environmental concerns due to the increase of heavy and toxic elements in the environment [2,3] that led to the subsequent legislations that restrict the use of toxic elements, including lead, in electronic and electrical devices [4,5]. Therefore, developing lead-free ceramic materials to replace $(Pb(Zr_xTi_{1x})O_3$ (PZT) in commercial electronic devices has become one of the pressing issues in the piezoelectric community. The BZT—BCT is one of the most promising alternatives, especially for room temperature piezoelectric applications. The processing-microstructure-functional properties relationship has been extensively investigated in BZT—BCT bulk ceramics [6–8]. However, macroscopic electromechanical properties of the thin film form of this material, suitable for microelectromechanical systems, are insufficiently reported. Furthermore, the mechanism of microstructure evolution in BZT—BCT thin films is still to be investigated. It is known that in chemical solution deposition (CSD) of thin films, the columnar grain growth is favorable in materials that crystallize via heterogeneous nucleation, such as PZT [9,10]. In contrast, granular equiaxed grains evolve in the films that crystallize via homogeneous nucleation, such as $BaTiO_3$ (BT) [11]. Nevertheless, it has been shown that columnar grains can be achieved in BT films by diluting the concentration of the coating solution and multistep annealing [12,13]. In our earlier study, we have also demonstrated that the columnar microstructure can be achieved in BZT—BCT thin films by CSD [14,15]. Functional properties, such as dielectric, ferroelectric/piezoelectric properties, are dependent on the thin-film microstructure. These properties are a few times higher in BZT—BCT thin films with columnar microstructure than in the films with equiaxed grains [14].

Higher functional properties in BT, $SrTiO_3$, and $(Ba,Sr)TiO_3$ (BST)

* Corresponding authors at: Jožef Stefan Institute, Jamova cesta 39, Ljubljana 1000, Slovenia.
E-mail addresses: sabi.william.konsago@ijs.si (S.W. Konsago), barbara.malic@ijs.si (B. Malič).

https://doi.org/10.1016/j.jallcom.2025.185124
Received 29 August 2025; Received in revised form 29 October 2025; Accepted 17 November 2025
Available online 20 November 2025

thin films with preferred crystalline orientation than in randomly oriented films have been reported [16–18]. In BST thin films deposited on platinized silicon, the preferred orientation was thought to be related to the orientation of the Pt (111) that served as a template. A variation of the preferred orientation as a function of the film thickness in BT thin films prepared by pulsed laser deposition was reported [19]. In that case, it was believed that the change in the orientation was related to the substrate influence and the different growth rate of grains with different orientations, depending as well on the oxygen pressure during deposition. So, it is important to understand and establish the mechanism of columnar grain growth and crystalline orientation in the BZT—BCT thin films on platinized sapphire substrates prepared by CSD.

Macroscopic electromechanical properties of 120 nm BZT—BCT thin films on platinized silicon substrates prepared by CSD and multi-step annealed at 850°C, were reported in our earlier study [14]. However, further increase of the film thickness resulted in the appearance of intergranular cracks, thus not allowing the investigation of macroscopic piezoelectric properties of thicker films, which are required in some applications, such as actuators [20,21]. By introducing platinized sapphire substrates with a thermal expansion coefficient (TEC) closer to that of BZT—BCT instead of platinized silicon, and thus reducing the thermal expansion mismatch, we prepared BZT–BCT films with thicknesses of up to 340 nm [22]. With the aim to further increase the film thickness, we managed to prepare crack-free 680 nm thick BZT–BCT films on platinized sapphire substrates by multistep annealing. The mechanism of columnar grain growth that leads to preferential crystallographic orientation, and dielectric, ferroelectric, and electromechanical properties of the films are discussed.

2. Experimental part

The manganese-doped $0.5(Ba(Zr_{0.2}Ti_{0.8})O_3—0.5(Ba_{0.7}Ca_{0.3})TiO_3$ (BZT—BCT) coating solution with 0.1 M concentration is prepared from alkaline earth acetates (barium acetate with a purity of 99.97 %, and calcium acetate with a purity of 99.999 %, purchased respectively from Sigma-Aldrich, St. Louis, Missouri, USA and Alfa Aesar, Karlsruhe, Germany), transition metal alkoxides (zirconium butoxide with a purity of 99.61 % and titanium butoxide with a purity of 80 % both purchased from Alfa Aesar, Karlsruhe, Germany). Ethylene glycol with a purity of 99.8 % (Sigma-Aldrich, St. Louis, Missouri, USA) and ethanol with a purity of 99.9 % (Sigma-Aldrich, St. Louis, Missouri, USA) are the respective solvents for acetates and alkoxides. Manganese acetate with a purity of 98 % (Alfa Aesar, Karlsruhe, Germany) is dissolved in the ethylene glycol solution in the amount of 1 mol% before mixing the acetates and alkoxides solutions. The Mn doping was introduced to reduce the leakage current [14]. The detailed solution preparation procedure was reported in our earlier work [15,22] and is described in the Supplementary Material S1. The preparation of the platinized sapphire substrate (Pt/Sapp) includes the atomic layer deposition (TFS-200, Beneq, Espoo, Finland) of 23 nm thick HfO_2 on a 500 μm thick C-sapphire (c-(0001) crystallographic plane) wafer (Siegert Wafer, Aachen, Germany). Finally, the top 100 nm thick platinum was deposited on the HfO_2 layer by rf sputtering (MED-020, Bal-tec Leica, Wetzlar, Germany).

The BZT—BCT thin film was deposited on the Pt/Sapp by spin coating (WS −400B-6NPP/ LITE, Laurell, North Wales, Pennsylvania, USA) for 30 s at 3000 rpm. The wet film was dried at 250 °C for 15 min, pyrolyzed at 350 °C for 15 min, and then the obtained amorphous film was annealed at 850 °C in the synthetic air with the heating and cooling rates of 13.3°C and 2.5°C per second, respectively. The processes of deposition, drying, pyrolysis, and annealing were repeated 60 times to prepare the film with the desired thickness. The annealing time was kept for 15 min for the first and last layers, whereas the annealing time of the intermediate layers was 5 min to reduce processing time.

A high-resolution diffractometer (X'Pert PRO, PANalytical, Almelo, The Netherlands) with Cu Kα radiation was used for XRD in the 2 theta ranges of 10–39 ° and 40–65 ° to avoid recording the Pt (111) peak of the substrate. The recording conditions were 0.016 step, 100 s per step, mask 10, and Soller slit 0.02. The XRD raw data were analyzed using X'Pert High Score Plus software.

Scanning electron microscopy (SEM) was conducted using a Verios 4 G HP field emission system (Thermo Fisher Scientific, Waltham, MA, USA). Surface imaging of the BZT—BCT film was performed at an accelerating voltage of 5 kV. Prior to SEM analysis, the film surface was coated with a 5 nm thick carbon layer using a Precise Etching and Coating System 628 A (Gatan, Pleasanton, CA, USA) to mitigate charging effects. Plan-view SEM images were used to determine the average grain size via the linear intercept method, based on measurements of 453 grains.

Electron-transparent cross-sectional lamella was prepared from the BZT—BCT film using a focused ion beam (FIB) system Helios Nanolab 650 HP (Thermo Fisher Scientific, Waltham, MA, USA) equipped with a Ga^+ ion source and a carbon gas injection system. Scanning transmission electron microscopy (STEM) on the cross-sectional lamella was performed using the annular STEM 3 + detector at 30 kV in the SEM Verios 4 G HP.

Crystallographic orientation analysis was performed using an Apreo 2 S field emission SEM (Thermo Fisher Scientific, Waltham, MA, USA) equipped with a C-Swift+ CMOS camera (Oxford Instruments, Abingdon, United Kingdom). Electron backscatter diffraction (EBSD) was conducted on the film surface at a 70° tilt and a beam energy of 20 kV. Transmission Kikuchi diffraction (TKD) was carried out on cross-sectional lamellae at a 20° tilt and a beam energy of 30 kV, using an off-axis TKD configuration. EBSD and TKD data were indexed using the Hough transform method assuming a cubic crystal system with a lattice parameter of 3.9 Å, corresponding to space group *Pm*-3*m* (No. 221).

For electrical measurements, gold electrodes with a 400 μm diameter were deposited on the top of the BZT—BCT film through a shadow mask by magnetron sputtering (5 Pascal, Trezzano sul Naviglio, Milan, Italy). The edge of the film was etched to reach the bottom platinum using the mixture of deionized water, HCl 37–38 % (J.T. Baker, Phillipsburg, New Jersey, USA), and HF 40 % (Alfa Aesar, Karlsruhe, Germany) in a volume ratio of 20:5:2, respectively.

The dielectric properties were measured at different frequencies as a function of temperature from −50 °C to 150 °C by an impedance analyzer (HP 4284 A, Keysight, Santa Rosa, USA).

The ferroelectric polarization loops and strain as a function of electric field, the piezoelectric coefficient d_{33}, the dielectric permittivity as a function of electric field were measured at 1 kHz by a double-beam laser interferometer (DBLI, Aixacct Systems GmbH, Aachen, Germany).

3. Results and discussion

The XRD of the BZT—BCT film reveals that the film crystallized in pure perovskite phase with a low crystallographic (111) texture ($f_{(111)}$ is 0.228, for details see Supplementary Material S2). The cross-sectional microstructure of the film investigated by SEM and STEM shows the BZT—BCT film with preferentially columnar grains across the thickness of about 680 nm, Fig. 1a, c, and d. The plan-view image shown in Fig. 1b) reveals a dense and crack-free surface microstructure. The preparation of a crack-free BZT—BCT film with such high thickness was enabled by a relatively small difference in the thermal expansion coefficient (TEC) between the film and the sapphire substrate. The respective TECs are $\sim 12 \times 10^{-6}$ K^{-1} and $\sim 8 \times 10^{-6}$ K^{-1} [23,24]. Note that BZT—BCT films deposited on platinized silicon substrates and annealed at 850 °C contain intergranular cracks at a thickness of about 120 nm, which is related to a large TEC mismatch between the film and the substrate [14]. The TEC of the silicon is about 3×10^{-6} K^{-1} [24].

The lateral grain size obtained by image analysis is 140 nm. By comparing this value with the grain sizes of thinner BZT–BCT films on platinized sapphire substrates and annealed at the same temperatures from our earlier study [22], namely 58 nm and 92 nm for the 100 nm and 340 nm thick BZT–BCT films, we observe the trend of increasing

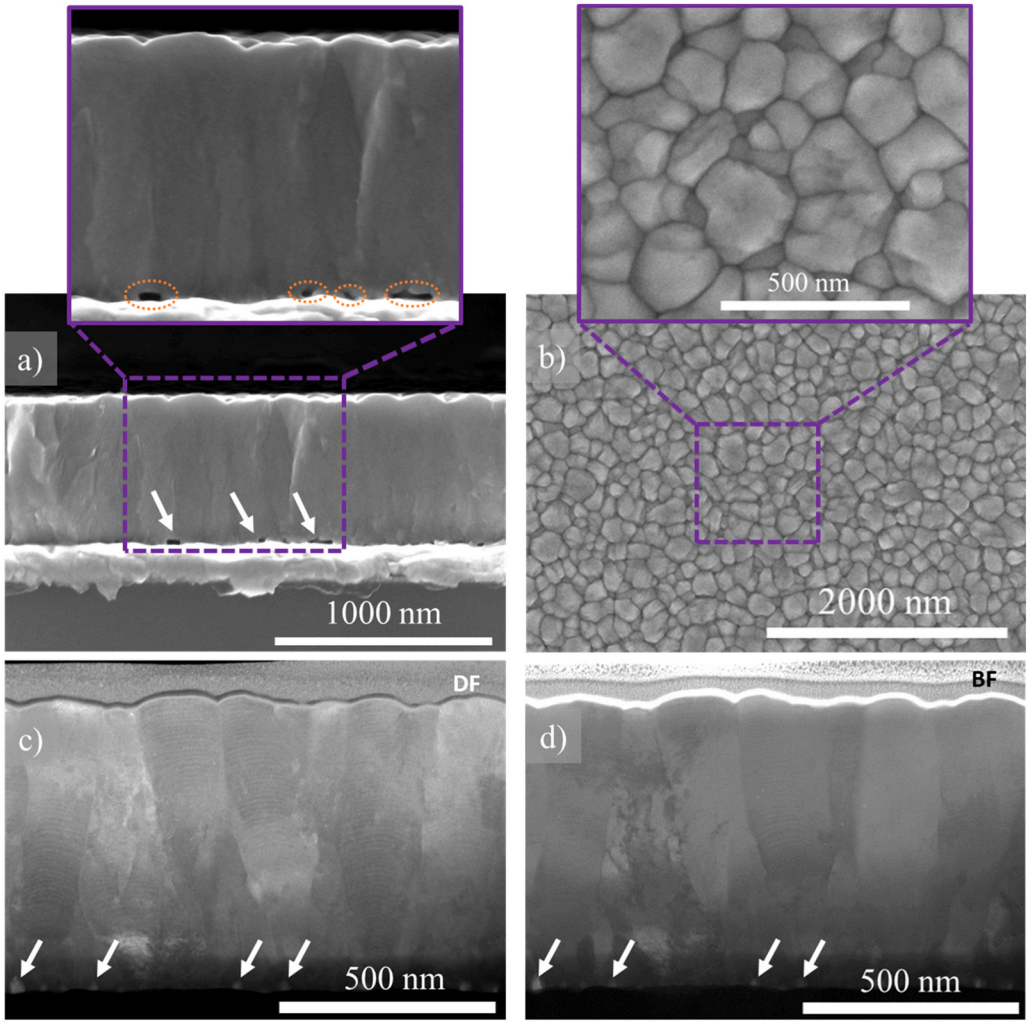

Fig. 1. SEM cross-section (a) and plan-view (b) micrographs of the BZT—BCT thin film. Outset images show magnified sections of the cross-section and plan-view micrographs. Dark field (DF) STEM (c) and bright field (BF) STEM (d) images. The white arrows indicate the position of the pores in (a), (c), and (d). The circles in the outset of the (a) image indicate the pores.

grain size with increasing film thickness. For comparison, see also Supplementary Material S3 Figure S2. Such a phenomenon was previously observed in $(Ba_{0.5}Sr_{0.5})TiO_3$ films [25–27] and related to the coarsening of grains during the multistep annealing.

In cross-sections of both SEM and STEM images shown in Fig. 1a, c, and d, small pores are present at the interface between the film and the substrate. This phenomenon could be related to the mobility of grain boundaries and pores [28,29]. With increasing film thickness, the pores

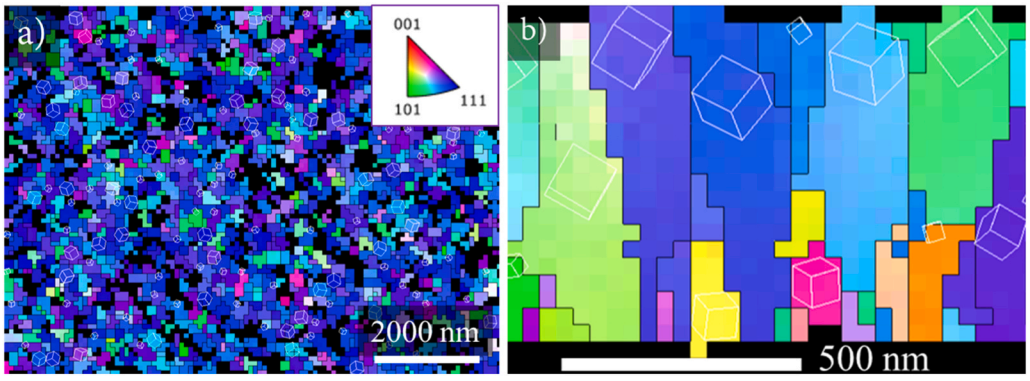

Fig. 2. Crystallographic orientation analysis is shown using IPFs. The image a) presents EBSD data with the IPF aligned along the Z-direction (surface normal, grain growth direction), while the image b) displays TKD data from the cross-section, with the IPF oriented along the Y-direction (grain growth direction). Grain boundaries with misorientation angles of 2° or greater are highlighted with black lines. The colored triangle inset in the plan-view image represents the standard IPF color key, indicating the crystallographic orientation of individual grains. A schematic of the cubic unit cell is overlaid on every grain to graphically view the orientation.

are dragged alongside grain boundaries and are accumulated at the interface with the substrate due to the different migration kinetics of grains and pores [30,31].

The crystallographic orientation analysis (Figure S3, Supplementary Material S4) provided insight into the mechanism of the columnar grain growth in the BZT—BCT film. The EBSD inverse pole figure (IPF) image of the film surface shown in Fig. 2a reveals the {111} preferred orientation. This result is in agreement with the earlier reported grazing angle and pole figure measurement of a 120 nm thick BZT—BCT film on Pt/Si substrate [14]. The TKD IPF image of the cross-section in Fig. 2b, however, shows a rather complex crystallographic structure of the film. At the bottom of the film, no preferential orientation can be observed, which agrees with our previous work on BZT—BCT thin films on platinized sapphire substrates. Indeed, no preferential orientation was observed in the 100 nm and 340 nm thick BZT—BCT films [22]. However, as evident in Fig. 2b, at a thickness of about 250 nm from the substrate, the grains with {111} and {110} orientations grow in both lateral direction and upwards, while other grains with different orientations almost stop growing. The crystallites with different orientations compete in the growth process. The fastest-growing crystallites with {111} and {110} orientations grow at the expense of the crystallites with other orientations. As a result, at the top of the film, the grains with predominant {111} orientation are observed, in agreement with Fig. 2a. The phenomenon of grain growth with a preferential crystalline orientation was modelled for polycrystalline thin films grown by vapour deposition [32–34].

We compare the microstructure evolution of BZT—BCT films with the well-understood cases of PZT and BT thin films, as shown in Fig. 3. The PZT films crystallize via heterogeneous nucleation, where the nuclei preferentially form on the substrate, serve as the nucleation layer, and grow towards the top of the film, resulting in a columnar microstructure [11]. BT thin films, in contrast, crystallize via homogeneous nucleation where the nuclei form within the bulk of the amorphous deposited film and grow until they impinge on neighboring grains, leading to a granular microstructure [11]. Note that the described mechanisms of both PZT and BT film growth occur in the single annealing step (SAS) processes. The BZT—BCT and BT thin films prepared by a SAS show a similar equiaxed grain and porous microstructure [35,36].

In BZT—BCT, as in BT, with a low concentration of the coating solution, the material crystallizes within one grain via the formation of one layer of nuclei with different orientations on the substrate due to the small amount of material deposited. The following layer crystallizes on top of the previous one, thus resulting in the columnar grain growth in a multi-annealing step (MAS) process [13,14]. However, nuclei with different orientations formed during the first deposition have different growth rates at a given temperature. During the multistep deposition and annealing, the grains growing in a favorable orientation occupy more space at the expense of the less-favorably oriented crystallites. As a result, the film develops a preferred orientation.

The temperature-dependent dielectric permittivity and losses are measured as a function of frequency from 33 Hz to 100 kHz and are

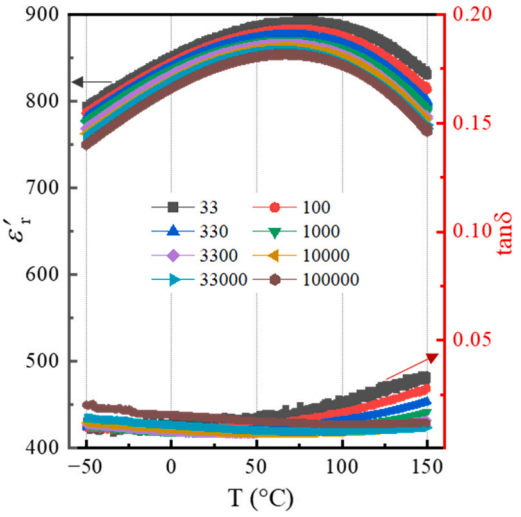

Fig. 4. Relative dielectric permittivity and losses of 680 nm thick BZT—BCT film measured as a function of (a) frequency and (b) temperature.

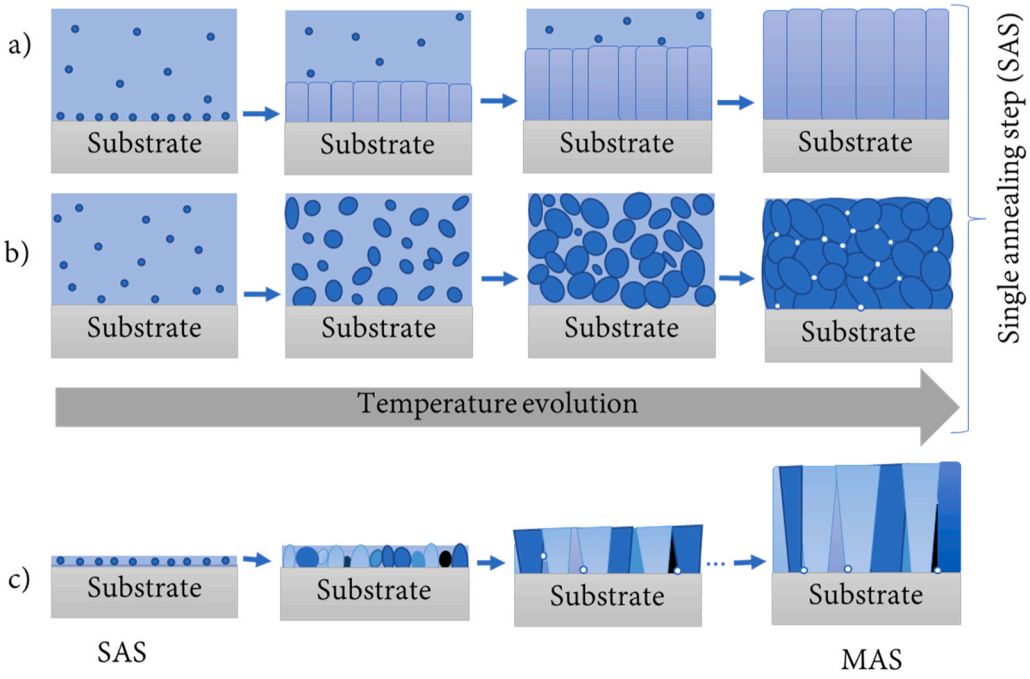

Fig. 3. Mechanism of heterogeneous nucleation and growth that leads to columnar microstructure of PZT thin films (a), homogeneous nucleation and grain growth that leads to granular microstructure of BT thin films (b) in single annealing step (SAS) processes. The engineered heterogeneous nucleation via multiple deposition-annealing steps (MAS) that lead to columnar microstructure of BZT—BCT thin films (c). The white spots in sketches b) and c) represent pores.

shown in Fig. 4. The values of the relative permittivity and losses at 1 kHz are 840 and 0.02, respectively, at about 20 °C, which is similar to the reported values in our previous work on 340 nm thick BZT—BCT films on Pt/Sapp (820 and 0.02, respectively) [22]. Note that the relative permittivity (157–280) of BZT—BCT thin films on Pt/Si substrate with fine grains and thickness ranging from 200 nm to 450 nm reported in the literature is 3–5 times lower [35,37,38]. We relate the high relative dielectric permittivity in our BZT—BCT to the grain size effect [39–41].

The dielectric permittivity measured as a function of temperature shows a broad transition peak in the temperature range between 60 °C and 90 °C, as shown in Fig. 4, which is much higher than the transition peak of the 340 nm thick film at 40 °C—50 °C reported in our earlier work [14]. This upshift may be related to stress relaxation in the thicker film. It has been reported that the tensile stresses in thin films decrease with increasing film thickness in BST and $Ba(Sn_{0.15}Ti_{0.8})O_3$ [27,42]. Note that the Curie temperature (T_C) of BZT—BCT bulk ceramic is around 85 °C, depending on the grain size [6].

The macroscopic electric field-dependent properties were measured by double-beam laser interferometry (DBLI) at room temperature. Fig. 5 shows the polarization coupled with strain as a function of electric field (a) and the dielectric tunability and piezoelectric coefficient d_{33} (b). The maximum polarization and strain measured up to the maximum electric field of 1.2 MV•cm^{-1} are 32 μC•cm^{-2} and 0.35 %, respectively, as shown in Fig. 5a. The low remanent polarization and coercive field of about 4 μC•cm^{-2} and 40 kV•cm^{-1}, respectively, align with earlier reported data of ferroelectric properties of BZT–BCT films on Pt/Sapp substrate, as well as their dielectric tunability [22]. However, the d_{33} in the 680 nm thick BZT—BCT film is about 42 pm•V^{-1}, which is about two times higher than the d_{33} of 120 nm thick BZT—BCT films deposited on Pt/Si substrate at the same conditions (concentration of coating solution, heating rate, and annealing temperature). This illustrates the dependence of the d_{33} on the film thickness and probably orientation and stress state in the films. Furthermore, note that the gold electrodes used for the measurement by DBLI have a diameter of 400 μm, while the substrate thickness is about 500 μm. It has been demonstrated that for the optimal and accurate d_{33} measurement, the ratio of the electrode diameter and the substrate thickness should be around 1 [43,44]. Therefore, the measured d_{33} value could be slightly underestimated due to the smaller size of the electrode. The corrected value of $d_{33,}$ considering the ratio of the electrode size to the thickness of the substrate around 1, is about 54 pm•V^{-1} (see Supplementary Material S5 for more details). The piezoelectric d_{33} coefficient of 42 pm•V^{-1} of the 680 nm thick film is comparable to the d_{33} of 40 pm/V measured in the 340 nm thick BZT—BCT film on the platinized sapphire [45].

To compare the macroscopic piezoelectric properties of the BZT—BCT thin film to other promising lead-free piezoelectric materials such as $(K_{0.5}Na_{0.5})NbO_3$ (KNN), $1–x(Bi_{0.5}Na_{0.5})TiO_3–xBaTiO_3$ (BNT–BT); the d_{33} measured by either DBLI, Laser Doppler Vibrometer (LDV), or laser scanning vibrometer (LSV) on different lead-free oxide thin films and deposited with different techniques including Pulsed Laser Deposition (PLD), RF Magnetron Sputtering (RF Sputt), CSD [14,46–52] is collected in Table 1. We note that we could not find the data for BZT–BCT films. Our BZT—BCT film shows a promising macroscopic $d_{33,}$ considering the film thickness is about 680 nm, which is up to a few times lower than the thickness of some films collected in Table 1. The use of $LaNiO_3/La_{0.5}Sr_{0.5}CoO_3$ (LNO/LSCo) or (LSCo/LNO) electrodes on Pt/Si substrates has contributed to achieving a high d_{33} reported in 1600 nm and 2000 nm thick (BNT–BT) films [50,52]. We speculate that the d_{33} in BZT–BCT films could be optimized by increasing the film thickness and/or introducing buffer layers on the Pt/Sapp substrates.

4. Summary

In summary, the microstructure and macroscopic piezoelectric properties of BZT—BCT thin films prepared by Chemical Solution Deposition were investigated. Crack-free 680 nm thick films crystallized in the perovskite phase. The crystallographic orientation analysis showed the preferential {111} orientation of the columnar grains at the film surface, presumably due to the fast growth of {111} crystallites compared to others. The dielectric permittivity as a function of temperature measured at different frequencies showed that the Curie temperature of such large-grained films is similar to the Curie temperature of the BZT—BCT bulk ceramic, with the frequency-dependent maximum dielectric permittivity of about 840 at 1 kHz at room temperature and reaching 900 at 33 Hz around the maximum dielectric permittivity peak. The maximum polarization and the electric field-induced strain are 32 μC•cm^{-2} and 0.35 %, respectively, at the maximum field of 1.2 MV•cm^{-1}. The effective macroscopic piezoelectric coefficient measured by DBLI is about 40 pm•V^{-1}, while the corrected value is 54 pm•V^{-1}. These results show a clear BZT—BCT microstructure evolution mechanism on platinized sapphire substrates and the macroscopic electromechanical properties, showing a great potential of BZT—BCT thin films among other lead-free materials for MEMS applications.

CRediT authorship contribution statement

Sabi William Konsago: Writing – review & editing, Writing –

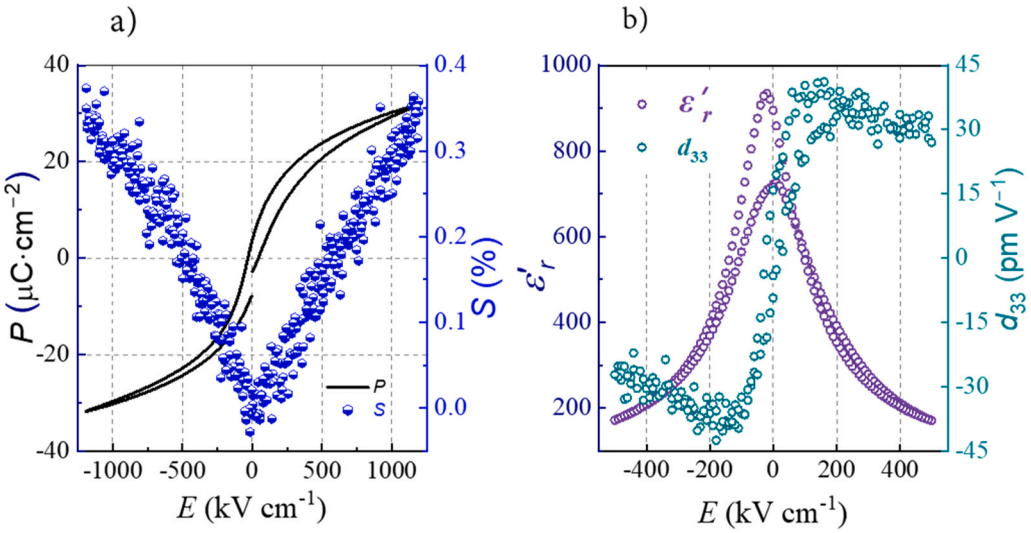

Fig. 5. Electric field dependence of (a) polarization and strain and (b) dielectric permittivity (ε_r') and small-signal piezoelectric d_{33} coefficient.

Table 1
The piezoelectric coefficient d_{33} of BZT—BCT (this work) and other lead-free perovskite oxide thin films prepared by different methods reported in the literature.

Materials	Substrate	τ, nm	Method	d_{33} meas. method	d_{33}, pm•V^{-1}	Ref
KNN	Pt/Si	750	PLD	DBLI	58	[46]
KNN	Pt/Si	1290	CSD	LSV	74	[47]
KNN	Pt/Si	1000	CSD	DBLI	90	[48]
KNN	LNO*/Si	600	RF Sputt	LDV	58	[49]
KNN	LNO/Si	600	RF Sputt	LDV	26	
BNT	Pt/Si	350	CSD	LDV	47	[51]
BNT-BT	LSCo**/LNO/Pt/Si	2000	PLD	LDV	220	[50]
BNT-BT	$SrRuO_3/SrTiO_3$/Si	1600	PLD	LDV	34	[52]
BNT-BT	LNO/LSCo**/Pt/Si	1600	PLD	LDV	275	
BZT-BCT	Pt/Si	120	CSD	DBLI	22	[14]
BZT-BCT	Pt/Sapp	680	CSD	DBLI	42	This work

* LNO: $LaNiO_3$,
** LSCo: $La_{0.5}Sr_{0.5}CoO_3$

original draft, Visualization, Validation, Methodology, Investigation, Formal analysis, Data curation, Conceptualization. **Maja Koblar Maja:** Writing – review & editing, Visualization, Methodology, Investigation, Formal analysis. **Aleksander Matavž:** Writing – review & editing, Visualization, Methodology, Investigation, Funding acquisition, Formal analysis. **Barnik Mandal:** Writing – review & editing, Visualization, Investigation, Formal analysis. **Katarina Žiberna:** Writing – review & editing, Visualization, Methodology, Investigation, Formal analysis. **Andreja Benčan:** Writing – review & editing, Visualization, Resources, Methodology, Funding acquisition, Conceptualization. **Barbara Malič:** Writing – review & editing, Writing – original draft, Visualization, Validation, Supervision, Resources, Methodology, Funding acquisition, Conceptualization. **Sebastjan Glinšek:** Writing – review & editing, Visualization, Methodology, Funding acquisition. **Vid Bobnar:** Writing – review & editing, Visualization, Resources, Funding acquisition.

Declaration of Competing Interest

The authors declare that they have no known competing financial interests or personal relationships that could have appeared to influence the work reported in this paper.

Acknowledgement

Slovenian Research and Innovation Agency (core funding P2–0105, J7–4637, P1–0125, S.W.K - young researcher programme, and MSCA-PF grant agreement n° 101110882. Barnik Mandal and Sebastjan Glinsek acknowledge the Luxembourg National Research Fund (FNR) for financial support through the project INTER/NWO/20/15079143/TRICOLOR. Dean Birmančević is acknowledged for his help related to the film deposition. Noureddine Adjeroud is acknowledged for ALD deposition of HfO_2.

Appendix A. Supporting information

Supplementary data associated with this article can be found in the online version at doi:10.1016/j.jallcom.2025.185124.

References

[1] W. Liu, X. Ren, Large piezoelectric effect in Pb-free ceramics, Phys. Rev. Lett. 103 (2009) 257602, https://doi.org/10.1103/PhysRevLett.103.257602.
[2] M.A. Hassanien, Atmospheric heavy metals pollution: Exposure and prevention policies in mediterranean basin, in: L.I. Simeonov, M.V. Kochubovski, B. G. Simeonova (Eds.), Environmental Heavy Metal Pollution and Effects on Child Mental Development, Springer, 2011, pp. 287–307, https://doi.org/10.1007/978-94-007-0253-0_17.
[3] M. Lagisz, R. Laskowski, Evidence for between-generation effects in carabids exposed to heavy metals pollution, Ecotoxicology 17 (2008) 59–66, https://doi.org/10.1007/s10646-007-0176-7.
[4] DIRECTIVE 2002/95/EC OF THE EUROPEAN PARLIAMENT AND OF THE COUNCIL of 27 2003 on the restriction of the use of certain hazardous substances in electrical and electronic equipment, ⟨http://data.europa.eu/eli/dir/2002/95/oj⟩. (accessed 28 October 2025).
[5] L.M. Benson, K.K. Reczek, A guide to United States electrical and electronic equipment compliance requirements, NIST Interag. /Intern. Rep. (2021), https://doi.org/10.6028/NIST.IR.8118r2.
[6] J. Hao, W. Bai, W. Li, J. Zhai, Correlation between the microstructure and electrical properties in high-performance $(Ba_{0.85}Ca_{0.15})(Zr_{0.1}Ti_{0.9})O_3$ lead-free piezoelectric ceramics, J. Am. Ceram. Soc. 95 (2012) 1998–2006, https://doi.org/10.1111/j.1551-2916.2012.05146.x.
[7] F. Benabdallah, et al., Structure–microstructure–property relationships in lead-free BCTZ piezoceramics processed by conventional sintering and spark plasma sintering, J. Eur. Ceram. Soc. 35 (2015) 4153–4161, https://doi.org/10.1016/j.jeurceramsoc.2015.06.030.
[8] H. Amorín, et al., Insights into the early size effects of lead-free piezoelectric $Ba_{0.85}Ca_{0.15}Zr_{0.1}Ti_{0.9}O_3$, J. Adv. Electron. Mater. 10 (2023) 2300556, https://doi.org/10.1002/aelm.202300556.
[9] W. Robert, Schwartz, Chemical solution deposition — Basic principles, in: D. M. Mitzi (Ed.), Solution Processing of Inorganic Materials, John Wiley & Sons, Inc, New Jersey, USA, 2009, pp. 33–76.
[10] S. Hoffmann-Eifert, T. Schneller, Orientation and microstructure design, in: T. Schneller, R. Waser, M. Kosec, D. Payne (Eds.), Chemical Solution Deposition of Functional Oxide Thin Films, Springer, Vienna, 2013, pp. 407–429, https://doi.org/10.1007/978-3-211-99311-8_17.
[11] R.W. Schwartz, T. Schneller, R. Waser, Chemical solution deposition of electronic oxide films, Comptes Rendus. Chim. 7 (2004) 433–461, https://doi.org/10.1016/j.crci.2004.01.007.
[12] S. Hoffmann, R. Waser, Control of the morphology of CSD-prepared $(Ba,Sr)TiO_3$ thin films, J. Eur. Ceram. Soc. 19 (1999) 1339–1343, https://doi.org/10.1016/S0955-2219(98)00430-0.
[13] S.W. Konsago, K. Žiberna, B. Kmet, A. Benčan, H. Uršič, B. Malič, Chemical solution deposition of barium titanate thin films with ethylene glycol as solvent for barium acetate, Molecules 27 (2022) 3753, https://doi.org/10.3390/molecules27123753.
[14] S.W. Konsago, et al., Engineering the microstructure and functional properties of $0.5Ba(Zr_{0.2}Ti_{0.8})O_3$ -$0.5(Ba_{0.7}Ca_{0.3})TiO_3$ thin films, ACS Appl. Electron. Mater. 7 (2024) 4467–4477, https://doi.org/10.1021/acsaelm.4c00530.
[15] S.W. Konsago, K. Žiberna, J. Ekar, J. Kovač, B. Malič, Designing the thermal processing of $Ba(Ti_{0.8}Zr_{0.2})O_3$ –$(Ba_{0.7}Ca_{0.3})TiO_3$ thin films from an ethylene glycol-derived precursor, J. Mater. Chem. C. 12 (2024) 14658–14666, https://doi.org/10.1039/D4TC02495H.
[16] T. Tohma, H. Masumoto, T. Goto, Microstructure and dielectric properties of barium titanate film prepared by MOCVD, Mater. Trans. 43 (2002) 2880–2884, https://doi.org/10.2320/matertrans.43.2880.
[17] K.A. Kazuhide Abe, S.K. Shuichi Komatsu, Dielectric constant and leakage current of epitaxially grown and polycrystalline $SrTiO_3$ thin films, Jpn J. Appl. Phys. 32 (9S) (1993) 4186, https://doi.org/10.1143/JJAP.32.4186.
[18] M. Izuha, K.A. Kazuhide Abe, N.F. Noburu Fukushima, Electrical properties of all-perovskite oxide $(SrRuO_3/Ba_xSr_{1-x}TiO_3/SrRuO_3)$ capacitors, Jpn J. Appl. Phys. 36 (9S) (1997) 5866, https://doi.org/10.1143/JJAP.36.5866.
[19] D.-Y. Kim, S.-G. Lee, Y.-K. Park, S.J.P. Soon Ja Park, Variation of the preferred orientation with thickness in barium titanate thin films prepared by pulsed laser deposition, Jpn J. Appl. Phys. 36 (12R) (1997) 7307, https://doi.org/10.1143/JJAP.36.7307.
[20] I. Kanno, Piezoelectric MEMS: ferroelectric thin films for MEMS applications, Jpn J. Appl. Phys. 57 (4) (2018) 040101, https://doi.org/10.7567/JJAP.57.040101.
[21] J. Liu, et al., Piezoelectric thin films and their applications in MEMS: a review, J. Appl. Phys. 137 (2025), https://doi.org/10.1063/5.0244749.
[22] S.W. Konsago, et al., High energy storage density and efficiency of $0.5Ba(Zr_{0.2}Ti_{0.8})O_3$ –$0.5(Ba_{0.7}Ca_{0.3})TiO_3$ thin films on platinized sapphire substrates, J. Mater. Chem. A 13 (2025) 2911–2919, https://doi.org/10.1039/D4TA05675B.
[23] S.W. Konsago, A. Debevec, J. Cilenšek, B. Kmet, B. Malič, Linear thermal expansion of $0.5Ba(Zr_{0.2}Ti_{0.8})O_3$-$0.5(Ba_{0.7}Ca_{0.3})TiO_3$ bulk ceramic, Inf. MIDEM J. Microelectron. Electron. Compon. Mater. 53 (2023) 233–238, https://doi.org/10.33180/InfMIDEM2023.403.
[24] W.M. Yim, R.J. Paff, Thermal expansion of AlN, sapphire, and silicon, J. Appl. Phys. 45 (1974) 1456–1457, https://doi.org/10.1063/1.1663432.

[25] W.-J. Lee, H.-G. Kim, S.-G. Yoon, Microstructure dependence of electrical properties of $(Ba_{0.5}Sr_{0.5})TiO_3$ thin films deposited on $Pt/SiO_2/Si$, J. Appl. Phys. 80 (1996) 5891–5894, https://doi.org/10.1063/1.363583.
[26] K. Kageyama, A. Sakurai, A. Ando, Y. Sakabe, Thickness effects on microwave properties of $(Ba,Sr)TiO_3$ films for frequency agile technologies, J. Eur. Ceram. Soc. 26 (2006) 1873–1877, https://doi.org/10.1016/j.jeurceramsoc.2005.09.090.
[27] T. Pečnik, S. Glinšek, B. Kmet, B. Malič, Combined effects of thickness, grain size and residual stress on the dielectric properties of $Ba_{0.5}Sr_{0.5}TiO_3$ thin films, J. Alloy. Compd. 646 (2015) 766–772, https://doi.org/10.1016/j.jallcom.2015.06.192.
[28] M. Verma, R. Mukherjee, Grain growth stagnation in solid state thin films: a phase-field study, J. Appl. Phys. 130 (2021) 025305, https://doi.org/10.1063/5.0049027.
[29] M.R. Tonks, P.-C.A. Simon, J. Hirschhorn, Mechanistic grain growth model for fresh and irradiated UO_2 nuclear fuel, J. Nucl. Mater. 543 (2021) 152576, https://doi.org/10.1016/j.jnucmat.2020.152576.
[30] J. Rödel, A.M. Glaeser, Pore drag and pore-boundary separation in alumina, J. Am. Ceram. Soc. 73 (1990) 3302–3312, https://doi.org/10.1111/j.1151-2916.1990.tb06453.x.
[31] J.D. Powers, A.M. Glaeser, Grain boundary migration in ceramics, Interface Sci. 6 (1998) 23–39, https://doi.org/10.1023/A:1008656302007.
[32] Paritosh, D.J. Srolovitz, C.C. Battaile, X. Li, J.E. Butler, Simulation of faceted film growth in two-dimensions: microstructure, morphology and texture, Acta Mater. 47 (1999) 2269–2281, https://doi.org/10.1016/S1359-6454(99)00086-5.
[33] A.J. Dammers, S. Radelaar, Two-dimensional computer modelling of polycrystalline film growth, Texture Stress Microstruct. 14 (1991) 757–762, https://doi.org/10.1155/TSM.14-18.757.
[34] O. Nilsen, O.B. Karlsen, A. Kjekshus, H. Fjellvåg, Simulation of growth dynamics in atomic layer deposition. Part II. Polycrystalline films from cubic crystallites, Thin Solid Films 515 (2007) 4538–4549, https://doi.org/10.1016/j.tsf.2006.11.024.
[35] W.L. Li, T.D. Zhang, D. Xu, Y.F. Hou, W.P. Cao, W.D. Fei, LaNiO3 seed layer induced enhancement of piezoelectric properties in (100)-oriented (1-x)BZT-xBCT thin films, J. Eur. Ceram. Soc. 35 (2015) 2041–2049, https://doi.org/10.1016/j.jeurceramsoc.2015.01.018.
[36] S.R. Reddy, A. Kumar, A.R. James, V.V.B. Prasad, S.K. Roy, Ferroelectric and nano-mechanical properties of the chemical solution deposited lead-free BCZT films, Mater. Sci. Eng. B 265 (2021) 115037, https://doi.org/10.1016/j.mseb.2020.115037.
[37] Q.G. Chi, C.H. Zhang, J. Sun, F.Y. Yang, X. Wang, Q.Q. Lei, Interface optimization and electrical properties of $0.5Ba(Zr_{0.2}Ti_{0.8})O_3$-$0.5(Ba_{0.7}Ca_{0.3})TiO_3$ thin films prepared by a sol-gel process, J. Phys. Chem. C. 118 (2014) 15220–15225, https://doi.org/10.1021/jp5036103.
[38] Q.G. Chi, et al., Microstructures and electrical properties of $0.5(Ba_{0.7}Ca_{0.3})TiO_3$-$0.5Ba(Zr_{0.2}Ti_{0.8})O_3$ thin films prepared by a sol-gel route, Ceram. Int. 39 (2013) 8195–8198, https://doi.org/10.1016/j.ceramint.2013.04.001.
[39] V. Buscaglia, et al., Grain size and grain boundary-related effects on the properties of nanocrystalline barium titanate ceramics, J. Eur. Ceram. Soc. 26 (2006) 2889–2898, https://doi.org/10.1016/j.jeurceramsoc.2006.02.005.
[40] J.F. Ihlefeld, A.M. Vodnick, S.P. Baker, W.J. Borland, J.P. Maria, Extrinsic scaling effects on the dielectric response of ferroelectric thin films, J. Appl. Phys. 103 (2008) 074112, https://doi.org/10.1063/1.2903211.
[41] S.M. Aygün, J.F. Ihlefeld, W.J. Borland, J.P. Maria, Permittivity scaling in $Ba_{1-x}Sr_xTiO_3$ thin films and ceramics, J. Appl. Phys. 109 (2011) 034108, https://doi.org/10.1063/1.3514127.
[42] S. Song, J. Zhai, L. Gao, X. Yao, S. Lu, Z. Xu, Thickness-dependent dielectric and tunable properties of barium stannate titanate thin films, J. Appl. Phys. 106 (2009) 024104, https://doi.org/10.1063/1.3181060.
[43] S. Sivaramakrishnan, P. Mardilovich, T. Schmitz-Kempen, S. Tiedke, Concurrent wafer-level measurement of longitudinal and transverse effective piezoelectric coefficients ($d_{33,f}$ and $e_{31,f}$) by double beam laser interferometry, J. Appl. Phys. 123 (2018) 014103, https://doi.org/10.1063/1.5019568.
[44] A. Matavž, A. Bradeško, T. Rojac, B. Malič, V. Bobnar, Self-assembled porous ferroelectric thin films with a greatly enhanced piezoelectric response, Appl. Mater. Today 16 (2019) 83–89, https://doi.org/10.1016/j.apmt.2019.04.008.
[45] S.W. Konsago, 2024. Microstructure design and multifunctionality of barium zirconate titanate-barium calcium titanate thin films prepared by chemical solution deposition [Doctoral dissertation, Institut Jožef Stefan, Ljubljana].
[46] M.D. Nguyen, M. Dekkers, E.P. Houwman, H.T. Vu, H.N. Vu, G. Rijnders, Lead-free $(K_{0.5}Na_{0.5})NbO_3$ thin films by pulsed laser deposition driving MEMS-based piezoelectric cantilevers, Mater. Lett. 164 (2016) 413–416, https://doi.org/10.1016/j.matlet.2015.11.044.
[47] P.C. Goh, K. Yao, Z. Chen, Lead-free piezoelectric $(K_{0.5}Na_{0.5})NbO_3$ thin films derived from chemical solution modified with stabilizing agents, J. Appl. Phys. Lett. 97 (2010) 102901, https://doi.org/10.1063/1.3488808.
[48] S.S. Won, et al., Lead-free Mn-doped $(K_{0.5},Na_{0.5})NbO_3$ piezoelectric thin films for MEMS-based vibrational energy harvester applications, J. Appl. Phys. Lett. 108 (2016) 232908, https://doi.org/10.1063/1.4953623.
[49] T. Li, G. Wang, K. Li, N. Sama, D. Remiens, X. Dong, Influence of LNO top electrodes on electrical properties of KNN/LNO thin films prepared by RF magnetron sputtering, J. Am. Ceram. Soc. 96 (2013) 787–790, https://doi.org/10.1111/jace.12047.
[50] K. Ishihama, et al., Achieving high piezoelectric performance across a wide composition range in tetragonal $(Bi,Na)TiO_3$ –$BaTiO_3$ films for micro-electromechanical systems, ACS Appl. Mater. Inter. 16 (2024) 1308–1316, https://doi.org/10.1021/acsami.3c13302.
[51] S.A. Dargham, et al., Synthesis and electrical properties of lead-free piezoelectric $Bi_{0.5}Na_{0.5}TiO_3$ thin films prepared by Sol-Gel method, J. Eur. Ceram. Soc. 38 (2018) 1450–1455, https://doi.org/10.1016/j.jeurceramsoc.2017.06.019.
[52] T. Shimizu, et al., Large piezoelectric response in lead-free $(Bi_{0.5}Na_{0.5})TiO_3$ -based perovskite thin films by ferroelastic domain switching: beyond the morphotropic phase boundary paradigm, ACS Appl. Mater. Inter. 13 (2021) 57532–57539, https://doi.org/10.1021/acsami.1c15713.